20th Australasian Fluid Mechanics Conference
Perth, Australia
5-8 December 2016

Bubble entrainment in vertical plunging jets

H. Wang[1], N. Bertola[1] and H. Chanson[1]

[1]The University of Queensland
School of Civil Engineering, Brisbane QLD 4072, Australia

Abstract

This paper presents a physical study of air bubble entrainment in supported two-dimensional plunging jet flows. Detailed air-water flow measurements were conducted with (a) an ultra-high-speed high-definition camera for flow conditions close to the onset of air entrainment next to the intersection of impinging jet and receiving water body, and with (b) a dual-tip phase-detection probe at higher jet impact velocities. The mechanisms of air entrainment were depicted based upon bubble visualisation. The air-water flow properties in the turbulent shear layer below the impingement point were investigated for impact velocities from 2.5 to 7.4 m/s. The free-falling jet was characterised by relatively high turbulence level and pre-aeration. The significance of such inflow conditions on the air entrapment and diffusion in the pool is discussed.

Introduction

A water jet plunging into a pool of still water is a seminal self-aerated flow [1,2]. Air entrainment takes place at the plunge point when the impinging velocity exceeds a critical value [1,6,8], and bubbles are advected in large-scale turbulent structures into deep water before being dispersed or driven to free-surface by buoyancy. While the air entrainment regimes and bubble-turbulence interplay are of fundamental concerns to the fluid mechanics community, the associated enhancements in flow aeration, energy dissipation and fluid mixing may have major implication in industrial and environmental applications [9,11].

The bubble entrainment mechanisms at plunging jets were studied experimentally for a range of jet conditions (e.g. various fluid viscosities, jet speeds and disturbance levels), although most studies focused on circular jets [4,11]. The significance of impact velocity on air entrainment characteristics was evidenced in the literature, while the jet length and initial turbulence level played also important roles [15,16]. Physical studies of the bubbly flow region beneath the receiving water surface encompassed flow imaging, laser Doppler velocimetry, particle imaging velocimetry and phase-detection probes [2,3,7,12,13]. The physical data provided a better understanding of air entrainment and bubble transport regimes and were used for validation of computational multiphase flow models [9,14]. The bubble-turbulence interplay, however, has not been investigated in fine details at large physical scale, because of the complexity of air-water flow motion as well as the limitation of two-phase flow measurement techniques.

The present study focused on two-dimensional supported water jets impinging into a relatively large receiving water body at rest. At low approaching velocities, the entrainment of individual air bubbles and packets was documented. The air-water flow properties were measured with an intrusive phase-detection probe at higher inflow velocities. This paper presents the preliminary results, dealing with the bubble-turbulence interaction in plunging jet flows using advanced flow measurement and data processing techniques.

Experimental Apparatus and Flow conditions

Planar jets were produced by a 0.012 m × 0.27 m rectangular nozzle. A 0.35 m long full-width PVC sheet, with transparent side windows, extended from the nozzle, supporting the free-falling jet running into a water tank. The tank was 2.5 m long, 1 m wide and 1.5 m deep, built with glass walls and an overflow gate (Fig. 1). The nozzle and the jet support were set at 89° to the horizontal, to prevent jet detachment. Water was fed from a head tank for discharges smaller than 0.013 m^3/s, or by a high head pump for larger flow rates up to 0.037 m^3/s. The flow rate was measured with orifice/Venturi meters in the supply pipe. The flow meters were calibrated on site, and the conservation of mass was checked based upon jet thickness and velocity measurements.

A Phantom v711 ultra-high-speed camera, equipped with Carl Zeiss Planar T*85mm f1.4 lens, was used to record the bubble formation and behaviour. The camera operated at up to 22,000 fps with full HD resolution. Video movies were taken through the tank wall and jet support side window, with a depth of field of less than 20 mm. The phase-detection probe was a dual-tip conductivity probe. Both tip sensors were identical but of different lengths. Each sensor had a 0.25 mm diameter central electrode and a 0.8 mm outer diameter shield acting as external electrode. The two sensors were separated by 6.9 mm in the streamwise direction and by a 2 mm transverse separation. Their signal processing provided the void fraction, bubble count rate, time-averaged interfacial velocity, turbulence intensity and bubble size distributions. Both sensors were sampled simultaneously at 20 kHz for 90 s at each measurement location. In addition, the free-falling jet flow was also characterised using a Prandtl-Pitot tube (Ø = 3.2 mm) and a miniature total pressure sensor.

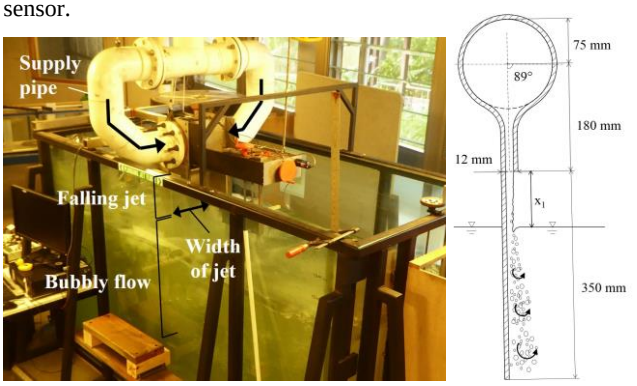

Figure 1. Plunging jet apparatus: photograph of jet nozzle and receiving water tank (left) and sketch of nozzle side view (right).

Table 1 summarises the flow conditions: series I corresponded to video observations and series II to air-water flow measurements. The experimental flow conditions were primarily characterised by the impact velocity V_1. The jet thickness d_1 was calculated from water-phase continuity for series I, and estimated as the equivalent air-water depth based on the void fraction measured in the jet at $x = x_1$ (series II).

Series	V_1 (m/s)	Q (m^3/s)	x_1 (m)	d_1 (m)	Re (-)	We (-)
I	1.00	0.0025	0.02	0.0094	9.4E+3	130
	1.12	0.0030	0.02	0.0099	1.1E+4	173
	1.26	0.0025	0.05	0.0074	9.4E+3	164
	1.36	0.0030	0.05	0.0082	1.1E+4	211
II	2.49	0.0067	0.10	0.0105	2.6E+4	904
	3.80	0.0114	0.10	0.0115	4.4E+4	2306
	5.55	0.0174	0.10	0.0127	7.0E+4	5433
	7.43	0.0236	0.10	0.0127	9.4E+4	9738

Table 1. Experimental flow conditions – Notation: V_1 impact velocity, Q flow rate, x_1 jet length, d_1 jet thickness at impingement, Re Reynolds number Re = $\rho \times V_1 \times d_1/\mu$, We Weber number We = $\rho \times V_1^2 \times d_1/\sigma$; Series I: video observations; Series II: air-water flow measurements.

Air Entrainment Mechanisms

For low-viscosity liquid jets, such as a water jet, the mechanism of air bubble entrainment varies from low-speed low-disturbance jet to high-speed high-disturbance jet [9,11]. The onset velocity above which air entrainment started to occur at the jet-pool intersection was found to be V_c = 0.9 m/s in the present study. Herein the bubble entrainment onset was defined when at least one bubble was entrained over 5 minutes as [8]. Such onset conditions corresponded to a critical Weber number $We_c \approx 100$ to 120, close to the findings of [8] but smaller than the minimum air-entrainment Weber number We_c = 400 proposed by [5] for short turbulent circular jets.

The number of entrained bubbles increased with increasing impact velocity $V_1 > V_c$. For impact velocities slightly larger than the onset air entrainment velocity (series I, Table 1), the entrainment of both individual bubbles and large air pockets was observed. The individual bubble entrapment took place almost randomly along the impingement perimeter, and was likely associated with the formation of an air layer next to the jet free-surface that intruded into the receiving water at the jet-pool intersection (Fig. 2a). The entrainment of large air pockets, on the other hand, was triggered by some disturbance in the jet, such as a jet surface roughness, that facilitated the formation of elongated air cavities at the impingement point (Fig. 2b). As the air cavity, or air finger, stretched in the streamwise direction, the lower part was pinched off, forming a detached air pocket that often broke quickly into several smaller bubbles. Meanwhile the upper part of the broken finger either shrank up at the free-surface or grew into a new finger. Figure 2 sketches the basic mechanisms of entrainment of individual bubbles and air pockets. Figure 3 illustrates the process of air pocket entrainment by a series of video frames.

The mechanisms of air finger/elongated cavity pinch-off were observed to be likely a combination of several factors: **(a)** surrounding pressure exerted on the finger perimeter that overcame the air-water surface tension as the finger elongated and surface curvature enlarged, **(b)** shear stress between the impinging flow and still plunge pool water that stretched and deformed the air cavity, **(c)** secondary current forming around the finger itself, similar to a whirlpool with a streamwise axis, that twisted the finger, and **(d)** unsteady flow recirculation induced by flow bulking and large-scale vortices, which induced instability of the flow field in the vicinity of impingement point. While single bubbles constituted the majority of entrained air entities at onset of air entrainment, the formation and detachment of elongated air cavities became the predominant air entrainment mechanism for larger impact velocities. Quantitative data are summarised in Table 2, showing an increasing percentage of entrained air pockets from 42% to 85% when the impact velocity V_1 increased from 1.00 to 1.36 m/s, together with a decrease in the proportion of single bubble entrapment from 17% to 7%.

Besides the above-mentioned air entrainment regimes, a number of entrained bubbles originated directly from the falling jet as well as from the water pool. The former mechanism is known as jet pre-aeration, although, in experiments series I, it was mostly linked to air-water exchange in the partially-filled pipeline feeding the jet nozzle. The latter mechanism was the re-entrainment of previously-entrained bubbles, rising towards the free-surface. These bubbles were driven into the shear layer by pressure gradient or large vortical structures before they reached the free-surface. Table 2 includes also the proportion of pre-entrained and re-entrained bubbles for different impact velocities (last row).

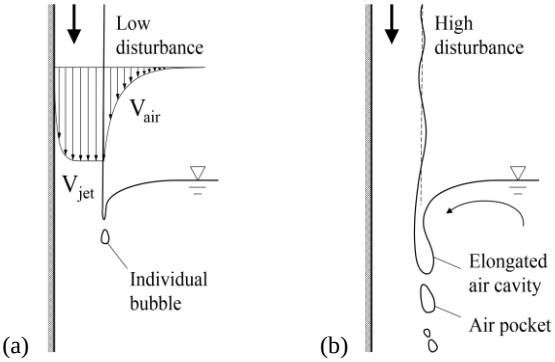

Figure 2. Air entrainment mechanisms for low disturbance jet (a. left) and high disturbance jet (b. right).

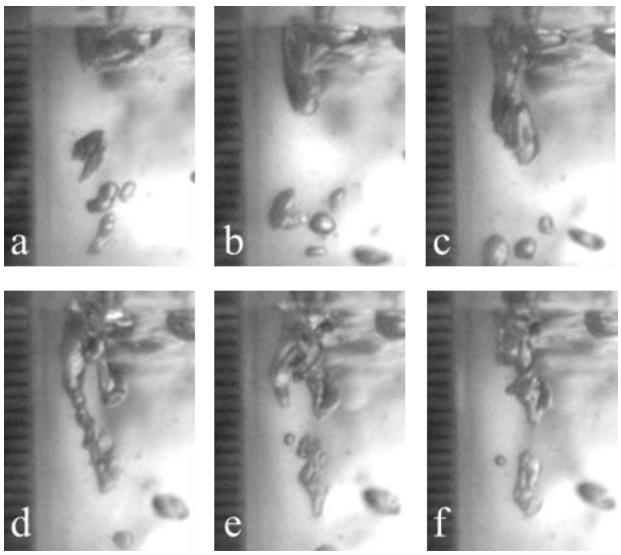

Figure 3. Air finger formation and air pocket pinch-off; flow conditions: V_1 = 1.26 m/s, x_1 = 0.05 m; shutter speed = 1/10,000; (a) t = 0s, (b) t = 0.012s, (c) t = 0.023s, (d) t = 0.033s, (e) t = 0.036s, (f) t = 0.040s.

Impact velocity V_1 (m/s):	1.00	1.36
Observation duration (s):	11.9	3.3
Total number of entrained bubbles/packets:	88	249
Proportion of single bubble entrapment (%):	17	7
Proportion of large air pocket entrainment (%):	42	85
Proportion of pre-aeration + re-entrainment (%):	41	8

Table 2. Effect of impact velocity on primary air bubble entrapment mechanisms.

Air-Water Flow in the Plunge Pool

Visually, the amount of entrained air increased substantially with increasing impingement velocity for $V_1 > V_c$ (series II, Table 1). A turbulent shear layer developed between the high-speed impinging flow and surrounding plunge pool (Fig. 1, right). A form of Kelvin-Helmholtz instability was visualised by the formation of large vortical structures in which air bubbles were

entrapped. The bubble transport in the shear layer was an advective diffusion process, until, further down the pool, stagnation took place and buoyancy became the dominant driving force.

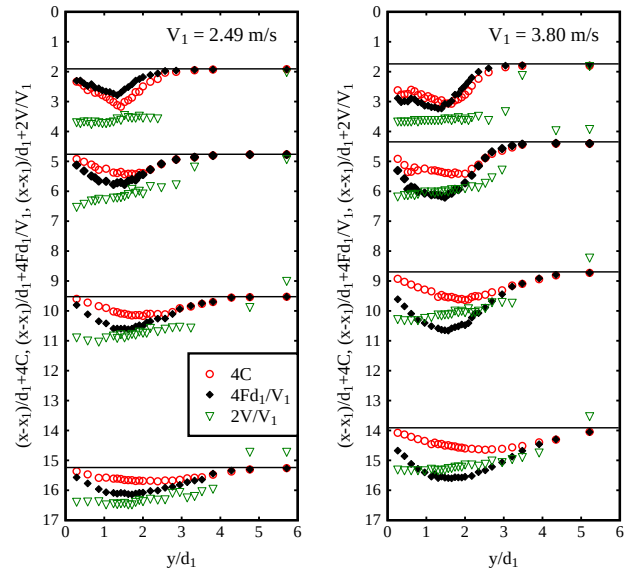

(a) V_1 = 2.49 m/s (b) V_1 = 3.80 m/s

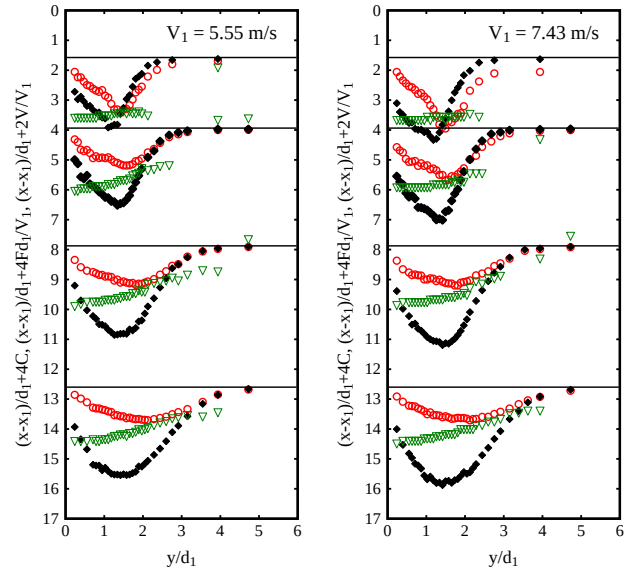

(c) V_1 = 5.55 m/s (d) V_1 = 7.43 m/s

Figure 4. Distributions of time-averaged void fraction, bubble count rate and interfacial velocity in the plunge pool; x_1 = 0.1 m; (a) V_1 = 2.49 m/s, (b) V_1 = 3.80 m/s, (c) V_1 = 5.55 m/s, (d) V_1 = 7.43 m/s.

Figure 4 presents typical distributions of time-averaged void fraction C, dimensionless bubble count rate $F \times d_1/V_1$ and time-averaged air-water interfacial velocity V/V_1 at different subsurface longitudinal cross-sections in the developing shear flow. In Figures 4a to 4d, the results are shown for various impact velocities with the same jet length x_1. Both void fraction and bubble count rate profiles exhibited a unimodal shape with a marked maximum, although the positions of maximum void fraction and maximum bubble count rate did not coincide because the air diffusion layer and the shear layer differ. The interfacial velocity profiles were quasi-uniform just below the impinging jet: i.e., $(x-x_1)/d_1 < 2$, $y/d_1 < 2.5$. Further downstream, a mixing layer took place, with momentum transfer from the high-velocity jet flow region to the plunge pool water at rest. No marked boundary layer was seen next to the jet support. Negative velocities were detected in the surrounding water, because of the presence of rising bubbles, for which the interfacial velocity was not equal to the water velocity.

The data indicated decreasing void fraction and interfacial velocity with increasing depth below the plunge point, as the flow was de-aerated and decelerated. However, an increase in maximum bubble count rate was seen for $0 < (x-x_1)/d_1 < 6$ to 10 before it decreased further downstream (Fig. 5b). Considering C×V/F being proportional to the average bubble size, the data trend reflected the breakup of large air pockets into small bubbles within $0 < (x-x_1)/d_1 < 6$ to 10 after entrapment. The streamwise evolution of maximum void fraction and bubble count rate is shown in Figure 5 and the present data are compared to the data of [3] who used smaller phase-detection probe sensors (Ø = 0.025 mm) and shorter sample duration (i.e. 3 s). For a similar impact velocity and identical jet length, previous data [3] showed remarkably larger bubble count rate. The discrepancy was believed to be primarily linked to the finer sensor size [3] allowing for detection of small bubbles with chord lengths between 0.025 and 0.25 mm. Such small bubble population had limited contribution to the local void fraction but significant impact on the bubble number, hence the total air-water interfacial area that affected the mass exchange between the two phases.

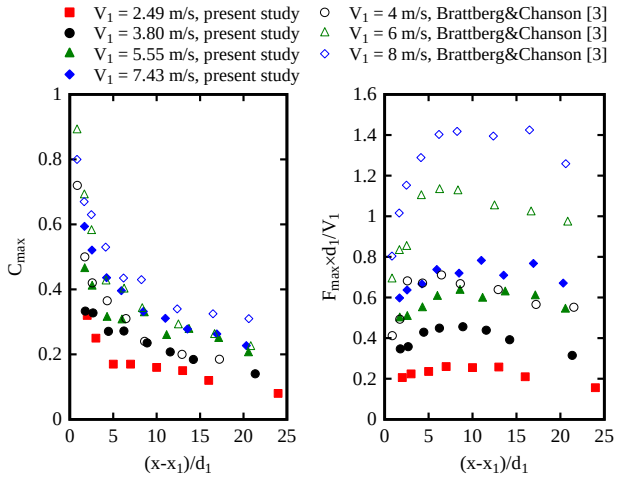

(a) Maximum void fraction (a) Maximum bubble count rate

Figure 5. Longitudinal distributions of maximum void fraction C_{max} (a. left) and maximum bubble count rate F_{max} (b. right) – Comparison with data of [3] for same jet length x_1 = 0.1 m.

Discussion: Inflow Turbulence and Air Entrainment

The inflow turbulence level is a key parameter affecting the air entrainment in plunging jet [8,12]. In the present study, the free-falling jet was characterised by a rough free-surface through which pre-aeration took place. The free-surface disturbance was linked to the development of air-water shear layer originating at the nozzle edge, and upstream turbulence of the nozzle itself (Fig. 1). Figure 6 shows a series of characteristics of the free-falling jet: void fraction, bubble count rate, velocity, free-surface fluctuations, and total pressure fluctuations. For a given jet velocity (V_1 = 7.43 m/s), the jet thickness fluctuations measured with acoustic displacement meters are presented in Figure 6a, and the velocity and total pressure data are shown in Figure 6b. The void fraction and bubble count rate in the jet are plotted for comparison. The mean jet thickness was larger than the theoretical value derived from mass and momentum conservation for clear-water because of the pre-aeration (Fig. 6a). The broadening of the free-surface air-water mixing layer was evidenced between the characteristic horizontal positions $y = Y_{10}$ and Y_{90} corresponding to void fractions of 0.1 and 0.9 respectively (Fig. 6a). The total pressure measurements were affected by the impact of air bubbles on the pressure sensor, and

the instantaneous pressure fluctuation was a superposition of velocity fluctuation and void fraction fluctuation (Fig. 6b). Taking into account the density change in air-water flow and assuming zero static pressure in the jet, the velocity turbulence intensity could be estimated at a first approximation using the difference between time-averaged total and kinetic pressure, yielding the turbulence intensity Tu in the order of 10^{-1}. The turbulence intensity results were found to be proportional to both fluctuation amplitudes of total pressure and local jet thickness.

The jet pre-aeration could further affect the plunging jet flow region below the impingement point. Considering Figure 5b the void fraction and bubble count rate profiles closest to the impingement point, a secondary peak is seen next to the jet support, corresponding to the pre-aeration bubbles. Such profile shapes were not observed in previous studies and implied unique inflow conditions of the present setup.

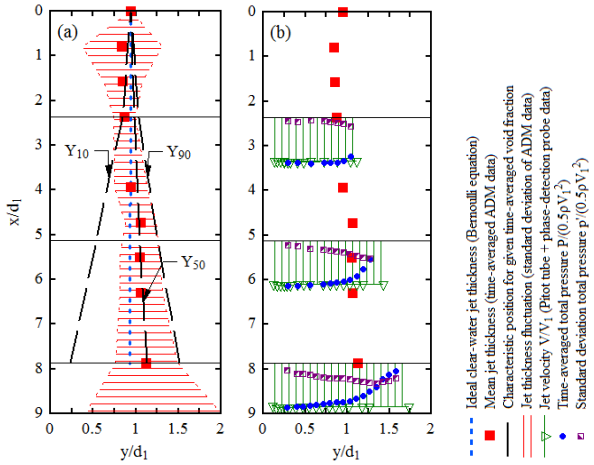

Figure 6. Dynamic characteristics of free-falling jet – two figures for the same jet with V_1 = 7.43 m/s.

Conclusion

New experiments were conducted to investigate the physical processes of air bubble entrainment in supported planar plunging jets, based on high-speed imaging and air-water flow measurements. Air entrainment took place for a minimum impact velocity of 0.9 m/s and Weber number of 100, with most air being entrained as individual bubbles. For slightly higher impact velocities, the pinch-off of elongated air cavities induced by large jet disturbance became the dominant air entrainment mechanism. At low impingement velocities from 0.9 to 1.36 m/s, the entrainment of distinct bubbles was observed and the formation, break-up and coalescence of air pockets were documented.

The air-water flow properties were measured with an intrusive phase-detection probe at higher impact velocities between 2.5 and 7.4 m/s, with intense air-water mixing downstream of the impingement point. The development of air diffusion layer and turbulent shear layer was characterised by the streamwise evolution of void fraction, bubble count rate and interfacial velocity profiles. Typical void fraction, bubble count rate and interfacial velocity profile shapes were consistent with the relevant literature, albeit the bubble count results were dependent on the phase-detection sensor size and the dynamic characteristics of impinging jet. The fluctuations of jet thickness, total pressure and jet velocity in the free-falling jet were coupled with some pre-aeration of the jet. The pre-entrained air affected the bubble distribution beneath the impingement point, in the close vicinity of singular aeration point at the jet-pool intersection.

Acknowledgments

The authors thank Jason Van Der Gevel (The University of Queensland) for manufacturing the phase-detection probe. The research is funded by Australian Research Council (Grant DP120100481) and the University of Queensland (School of Civil Engineering).

References

[1] Bin, A., Gas Entrainment by Plunging Liquid Jets, *Chem. Eng. Sci.*, **48**(21), 1993, 3585-3630.

[2] Bonetto, F. & Lahey, R. An Experimental Study on Air Carry under due to A Plunging Liquid Jet, *Int. J. Multiphase Flow*, **19**, 1993, 281-294.

[3] Brattberg, T. & Chanson, H., Air Entrapment and Air Bubble Dispersion at Two-Dimensional Plunging Water Jets, *Chem. Eng. Sci.*, **53**(24), 1998, 4113-4127.

[4] Chirichella, D., Gomez Ledesma, R., Kiger, K. & Duncan, J., Incipient Air Entrainment in a Translating Axisymmetric Plunging Laminar Jet, *Phys. Fluids*, **14**, 2002, 781-790.

[5] Ciborowski, J. & Bin, A., Minimum Entrainment Velocity for Free Liquid Jets, *Inz. Chem.*, **2**, 1972, 557-577(in Polish).

[6] Cummings, P.D. & Chanson, H., Air Entrainment in the Developing Flow Region of Plunging Jets – Part 1: Theoretical development, *J. Fluids Eng.*, Transactions ASME, **119**(3), 1997, 597-602.

[7] Cummings, P.D. & Chanson, H., Air Entrainment in the Developing Flow Region of Plunging Jets – Part 2: Experimental, *J. Fluids Eng.*, Transactions ASME, **119**(3), 1997, 603-608.

[8] Cummings, P.D. & Chanson, H., An Experimental Study of Individual Air Bubble Entrainment at a Planar Plunging Jet, *Chem. Eng. Research and Design*, Trans. IChemE, Part A, **77**(A2), 1999, 159-164.

[9] Ervine, D.A., Air Entrainment in Hydraulic Structures: A Review, *Proc. Instn Civ. Engrs Wat., Marit. & Energy*, **130**(Sept), 1998, 142-153.

[10] Galimov, A., Sahni, O., Lahey, R., Shephard, M., Drew, D. & Jansen, K., Parallel Adaptive Simulation of a Plunging Liquid Jet, *Acta Math. Sci.*, **30**, 2010, 522-538.

[11] Kiger, K. & Duncan, J., Air-Entrainment Mechanisms in Plunging Jets and Breaking Waves, *Annu. Rev. Fluid Mech*, **44**, 2012, 563-596.

[12] McKeogh, E. & Ervine, D.A., Air Entrainment Rate and Diffusion Pattern of Plunging Liquid Jets, *Chem. Eng. Sci.*, **36**, 1981, 1161-1172.

[13] Qu, X., Goharzadeh, A., Khezzar, L. & Molki, A., Experimental characterization of air-entrainment in a plunging jet, *Exp. Therm. Fluid Sci.*, **44**, 2013, 51-61.

[14] Richards, J., Lenhof, A. & Beris, A., Dynamic Breakup of Liquid–Liquid Jets, *Phys. Fluids*, **6**, 1994, 2640-2655.

[15] Soh, W., Khoo, B., Daniel, W. & Yuen, The Entrainment of Air by Water Jet Impinging on a Free Surface, *Exp. Fluids*, **39**, 2005, 498-506.

[16] Zhu, Y., Oguz, H. & Prosperetti, A., On the Mechanism of Air Entrainment by Liquid Jets at a Free Surface, *J. Fluid Mech.*, **404**, 2000, 151-1